Supporting Information: *Accurate Location and Manipulation of Nano-Scaled Objects Buried under Spin-Coated Films*

Colin Rawlings,[†] Heiko Wolf,[†] James Hedrick,[‡] Dan Coady,[‡] Urs Duerig,[†] and Armin Knoll[*,†]

IBM Research - Zurich, Rueschlikon 8803, Switzerland, and IBM Research - Almaden, San Jose, CA 95120 USA.

E-mail: ark@zurich.ibm.com

---

[*]To whom correspondence should be addressed
[†]IBM Research - Zurich
[‡]IBM Research - Almaden
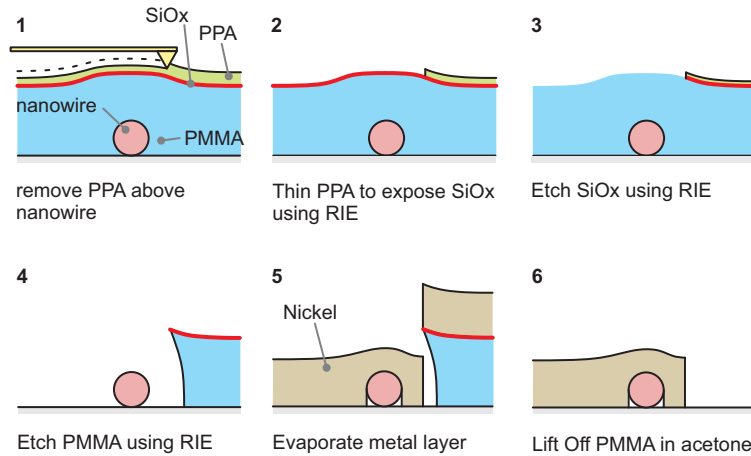
1

Contents

Details on pattern transfer

Figure S1: Process flow used to write electrodes to the nanowire using tSPL see ref. 1 for further details. The pattern is written into the PPA (Polypthaldehyde), a series of Reactive Ion Etches (RIE) are used to transfer this pattern into the layer of Polymethylmethacrylate (PMMA) ready for metallisation.

The process for copying a pattern written into the PPA layer into a final metal layer is shown in figure S1. To enable this pattern transfer it is necessary to first deposit a "transfer stack"[1,2] of [PMMA (60nm)| SiOx (4nm) | PPA (20nm)]. The PMMA and PPA are deposited

using spin coating. For the work reported here sputtering was used to deposit the SiOx layer although subsequent investigation has shown that it is preferable to evaporate the SiOx layer.

The next step, which is not shown in the figure, is to read the surface topography with the tip heater switched off. This allows for accurate measurement of the topography without exposing the resist. From this topography measurement the location of the buried nanowire can be identified. The desired electrode pattern is then generated and written into the PPA layer by the hot tSPL tip. The SiOx is then exposed by a short O_2/N_2 reactive ion etch (RIE) of the PPA layer. Next a CHF_3 etch is used to transfer the pattern into the SiOx layer. Finally an O_2 etch is used to transfer the pattern into the PMMA. From this point the process flow matches that which is used to perform conventional e-Beam liftoff. Further details including etch conditions are available in.[1]

Results for spin coating of the technically relevant organic hard-mask layer HM8006

Investigations into the film topography occuring when spin coating over sub-surface features were also performed on the commercial resist HM8006 manufactured by JSR Micro. In this study resist layers were successively added to samples containing the "wire grids" shown in figure S2a. The ability of the Gaussian model to fit the surface topography obtained after each stage of spin coating was examined. In this study the film properties were held constant while the sub-surface topography was varied since after each spin coating process the sample was more planar.

The topography was defined using optical lithography and transferred into Silicon using a Hydroflouric acid etch to measured depths of 56nm and 112nm. The same spin coating parameters and solution composition, which resulted in a 30nm thick layer was used for each spin coating stage. After each spin coating process the film was cured to cross-link the film, as such the existing film did not re-dissolve when the solution for the next spin coating
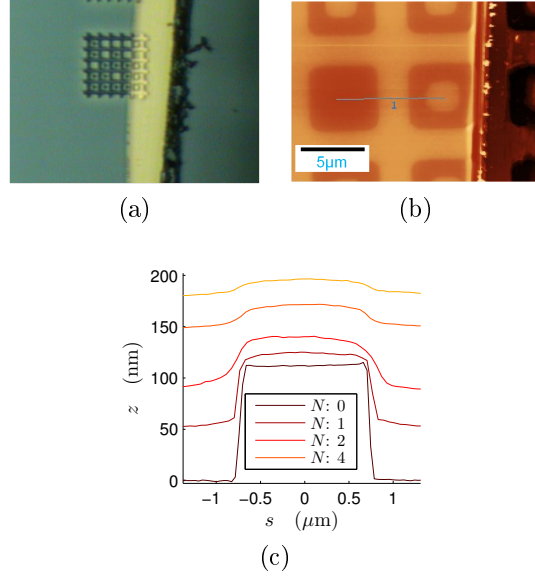
Figure S2: (a) Optical image of the pattern defined in Silicon and placed beneath the HM8006. A scratch test has been used to remove a portion of the polymer film. (b) AFM topography image in the vicinity of the scratch. (c) Height measurement along the cross-section in (b) following the addition of N layers of HM8006.

process was dispensed onto the sample. The film was scratched using a sharp scalpel (see figures S2a and S2b to determine its absolute thickness in the vicinity of the topographic features. The topography was measured using a Bruker Dimension V AFM. The evolution of topography with each stage of the spin coating process is shown in figure S2c.

It is important to note that the result of convolving a Gaussian with itself is also a Gaussian with a σ value which is $\sqrt{2}\sigma$ where σ is the parameter characterising the width of the original distribution. Thus if a single layer of a spin coated film is described by Kernel having parameters σ and R then according to the model developed in the main body of the text the N layer Kernel will have the parameters:

$$\sigma_N = \sigma\sqrt{N} \tag{S1}$$

$$R_N = R^N \tag{S2}$$

4

Results

Figure S2c shows topography measurements along a cross section which cuts one of the vertical wires in the pattern (see S2b) following the addition of N layers of the HM8006 resist. The result of convolving a Gaussian with an infinitely long wire of height t_p and in-plane width L_x has been used to fit the measured cross sections:

$$z = \frac{Rt_p}{2} \left[\mathrm{Erf} \left(\frac{x + L_x/2}{\sigma\sqrt{2}} \right) - \mathrm{Erf} \left(\frac{x - L_x/2}{\sigma\sqrt{2}} \right) \right] \tag{S3}$$

Results are shown for two different geometries, in the first the "wire" has a thickness t_p of 58nm and a nominal width $L_x = 2\mu$m whereas in the second $t_p = 112$nm and L_x=1.5μm. The fitting parameters are shown in figures S3c to S3e. The black dashed lines in figures S3d and S3e show a least squares fit of equations (S2) and (S1) to the experimental data.

The data shown in figure S3 is consistent with the predictions of the Gaussian convolution model with the exception of the results obtained for a single layer of HM8006. This is understandable given the large topography amplitude compared with the film thickness after the addition of only one layer. For subsequent spin coating steps where the sample has been partially planarised the agreement is good. Firstly the experimental topographies (figures S3a and S3b) are all well fitted by the model. Secondly, the fitted wire width L_x (figure S3c) does not appear to depend on the number of layers. Furthermore the dependence of the combined stack parameters σ_N and R_N (figures S3d and S3e) on N is well described by equations (S1) and (S2).

The behaviour observed here supports the Gaussian convolution model. Indeed the effectiveness of the model in describing the behaviour of topography amplitudes which are similar to that of the dry film thickness could not be readily anticipated from the limiting calculation pursued in the main text.
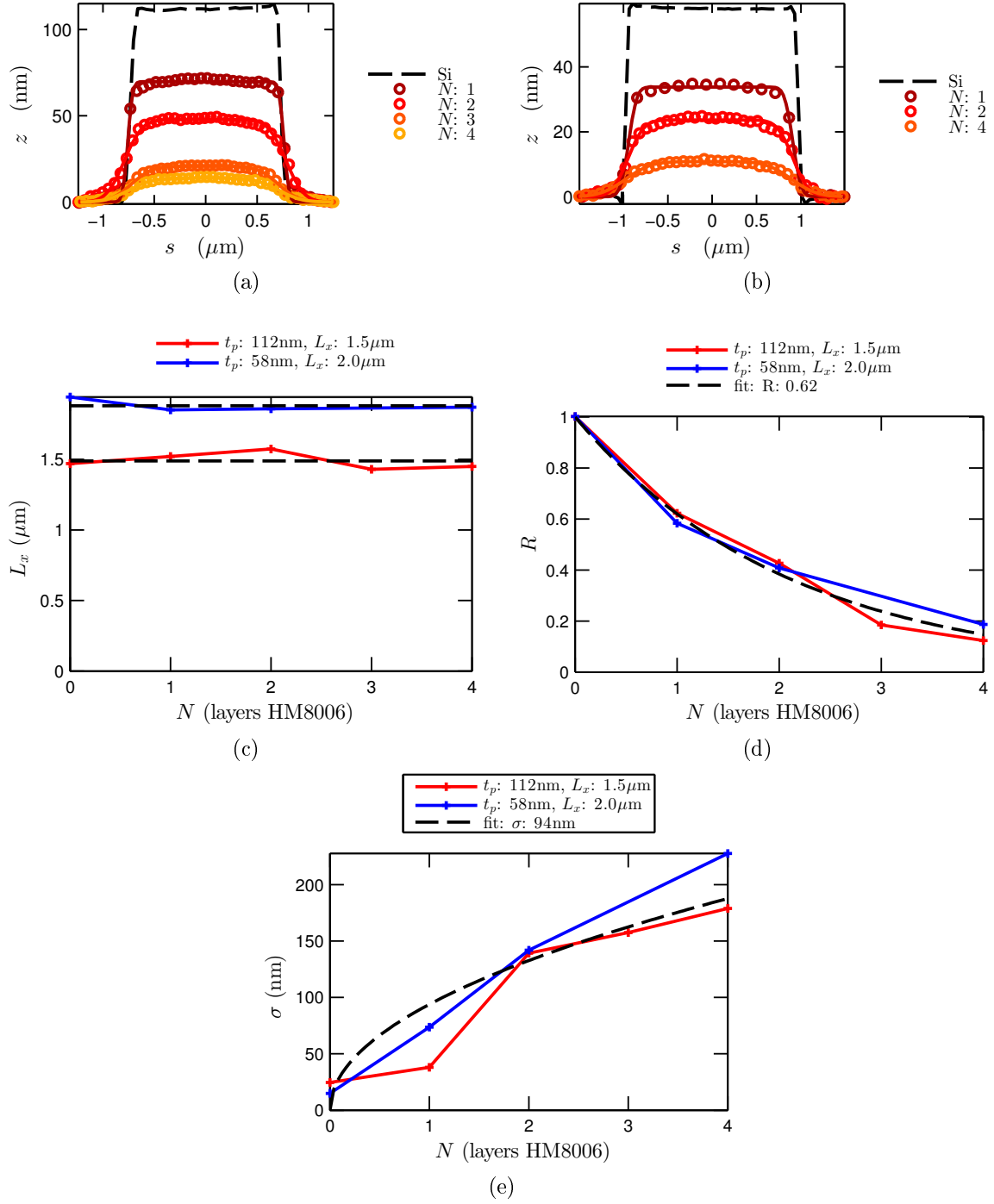
Figure S3: (a) Result of fitting the topography (line) on a cross section across a wire (see figure S2b) with the Gaussian convolution model (dots) (equation ((S3)) for a wire having a thickness $t_p = 58$nm and width $L_x = 2\mu$m. N is the number of layers added to the Silicon topography prior to taking the AFM measurement. (b) As for (a) with $t_p = 112$nm and $L_x = 1.5$ μm. (c) The dependence of the fit parameter describing the wire width L_x in equation (S3) on number of HM layers. (d) The dependence of the fit parameter R on the total number of HM layers. (e) The dependence of σ on the total number of HM8006 layers.

Alignment of figures 3a and 3b

To allow for the registration of the surface and sub-surface topography for the PMMA film the following steps were used:

1. Spin coat a PMMA film onto the silicon topography

2. Scratch the film with a sharp scalpel

3. Identify a field through which the scratch passed

4. Record the field with the tSPL tool (figure S4a).

5. Remove the PMMA film using acetone

6. Re-image the field in the tSPL tool (figure S4b).

7. Align the pair of images using cross-correlation. Only the scratched part of the image was used in the cross-correlation.
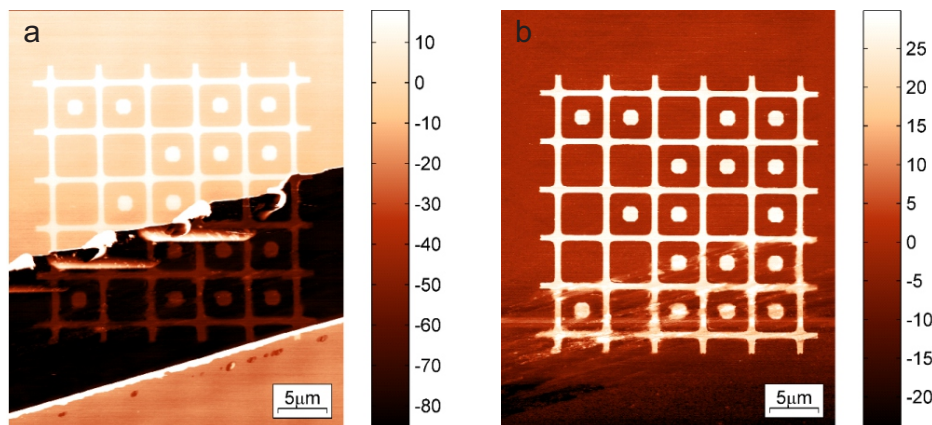
Figure S4: tSPL topography images of 30nm silicon features in the vicinity of area scratched using a sharp scalpel. The upper left hand portion of these images appeared in figures 3a and 3b in the main text. (a) Silicon topography underneath an 80nm spin-coated PMMA layer. Part of the film has been removed by scratching with a sharp scalpel. (b) Region in (a) following the removal of the remainder of the PMMA film using acetone.

Details on the measurement of the patterning overlay error using scanning probe lithography
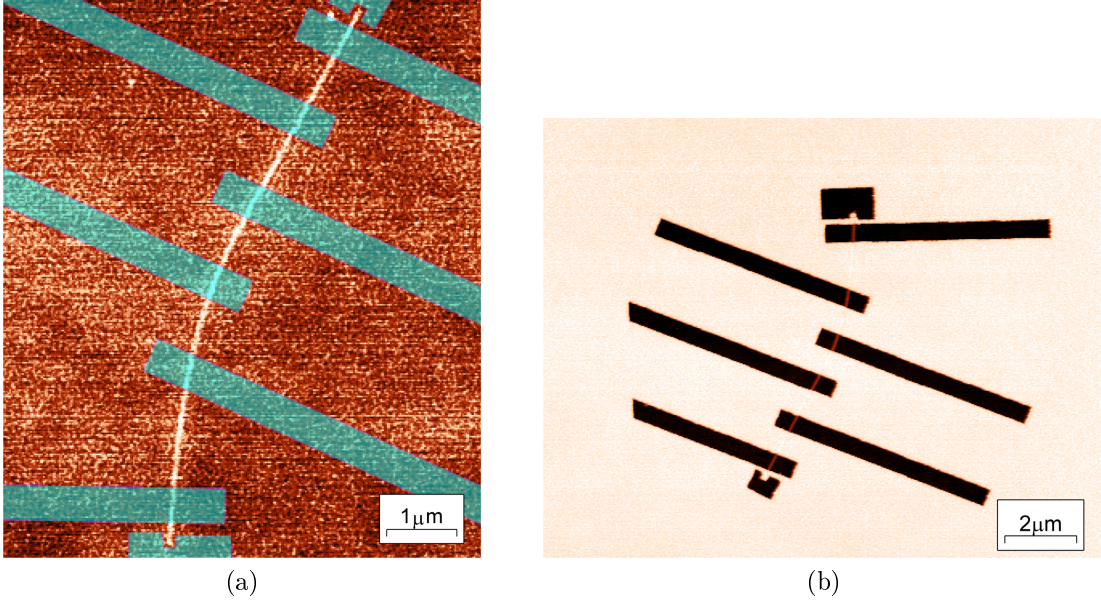

(a)   (b)

Figure S5: Images used to determine the error for the overlay process (a) The design of contact pads is shown in blue (z_c). The contact pads were drawn in `Inkscape` in registry with the imaged nanowire which is shown using the red-white colormap (z_{R1}), the pattern has an amplitude of 3nm. (b) AFM image of device area following pattern transfer via reactive ion etching into the PMMA layer (z_{R2}). The pattern has an amplitude of 64nm.

Calculation of the correlation error for the overlay process requires three images which are shown in figure S5.

1. The measured resist surface prior to patterning z_{R1} in which the nanowire is visible (see figure S5a). This image was measured in the tSPL tool.

2. The contact pad design z_c (see figure S5a) which was defined with respect to z_{R1} using the graphics package (INKSCAPE).

3. The topography following the transfer of the pattern into the PMMA z_{R2} (see figureS5b). In this image both the nanowire and the position of the contact pads are visible.

The overlay error for the tSPL lithography process was measured in two stages.

1. First z_{R2} was aligned with z_c. The algorithm described in[3] was used to identify the rotation, slow axis scaling and fast axis scaling that maximised the cross-correlation between the pair of images. This transformation was then applied to z_{R2} to yield z'_{R2}. Note that it was not necessary to perform this process for z_{R1} since this image is already aligned with z_c.

2. The error in the overlay was then measured by masking z'_{R2} so that only the portions of the nanowire visible at the bottom of the etched trenches in the PMMA were included in the image. We refer to this image as $z'_{R2,m}$. The overlay error was then obtained by calculating the cross correlation between z_{R1} and $z'_{R2,m}$.

The calculation was performed using the scripting language `Matlab`.

The optimisation algorithm identified the following transformation parameters as minimising the difference between z_c and z_{R2}:

$$\text{rotation} = 177.7°, \quad x \text{ axis scaling} = 98.1\%, \quad y \text{ axis scaling} = 1.05\%$$

We attribute the non-unity scaling observed here to two sources. The first is discrepancies in the calibration of the x-y Piezo scanners used in our tSPL tool and in the AFM. For the slow axis we expect an additional error source which is due to the drift that occurs during the scan period.

These transformation parameters were used to generate z'_{R2}. z'_{R2} was aligned with z_c using cross-correlation. Sub-pixel accuracy was achieved using direct DFT upsampling as outlined in ref.[4] A factor of $\times 100$ was used. The normalised cross-correlation for the pair of images is shown in figure S6a. A cross-section through this function is shown in figure S6b. The result of using this cross-correlation to align the images is shown in figure S6c.
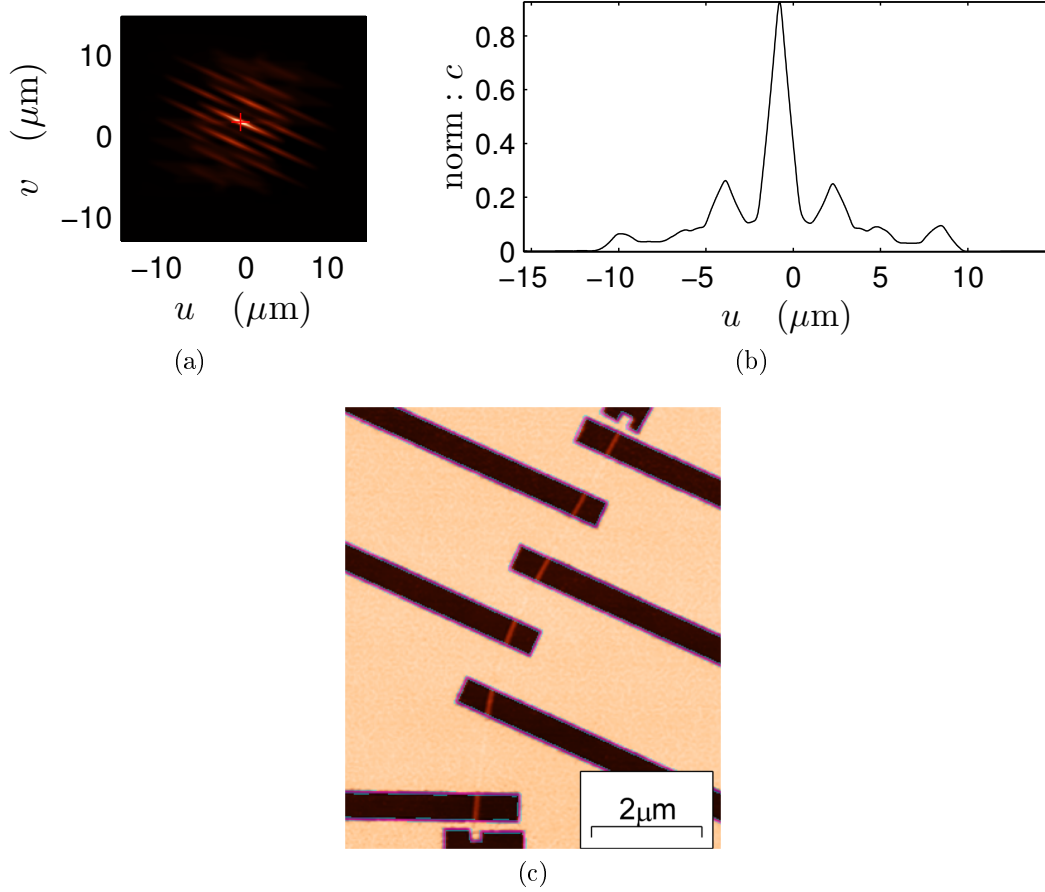
(a)

(b)

(c)

Figure S6: Result of using cross-correlation of the design for the contact pads z_c with the transformed AFM topography image z'_{R2}. z_{R2} is the surface topography following transfer of the written tSPL pattern transferred into the 60nm PMMA layer. (a) The cross correlation function for the images. The location of the peak in the cross correlation function is shown by the red cross. (b) A horizontal cross section through the correlation peak shown in (a). (c) The transformed PMMA topography image z'_{R2}. The purple lines were obtained by applying an edge detection (Sobel) filter to z_c and then overlaying the result onto z'_{R2}, zero valued pixels (non-edge pixels) were made transparent for clarity.

The final step of the analysis was to measure the offset in position between the nanowire in z_{R1} and the aligned copy of z'_{R2}. The mask as well as the resulting image $z'_{R2,m}$ are shown in figures S7a and S7b respectively.

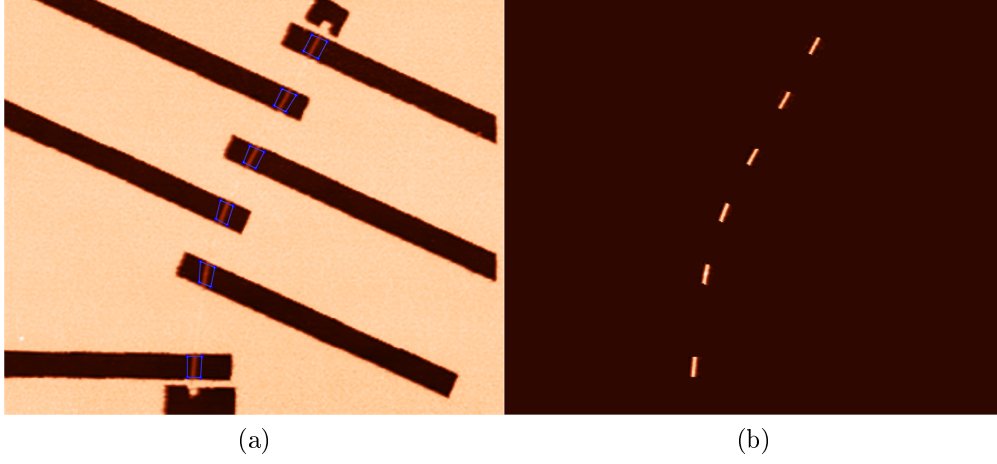(a)   (b)

Figure S7: The masked copy of z'_{R2} used to measure the overlay error. (a) An image of z'_{R2} with the areas included in the masked image shown with the blue blue polygons. The topography amplitude is 64nm. (a) The result of applying the mask of (a) to z'_{R2} to yield $z'_{R2,m}$, the topography amplitude is 27nm.

The cross-correlation function for z_{R1} and $z_{R2,m}$ is shown in figure S8a. A cross-section through this function is shown in figure S8b. The measured overlay error was obtained from the cross-correlation function as:

$$x = 20.1\text{nm}, \quad y : 47.8\text{nm} \tag{S4}$$

The result of aligning the pair of images by applying this offset is shown in figure S8c. If the axis of the nanowire is taken to be parallel to the line joining its two ends (the green dashed line in figure S8c) then this overlay error may be decomposed into components parallel and perpendicular to the nanowire to yield:

$$\text{perpendicular} : 2.9\text{nm}, \quad \text{parallel} : 51.8\text{nm} \tag{S5}$$

11

It may be observed in figure S8c that the overlay error is closely aligned with the axis of the nanowire. This result may be anticipiated intuitively and from the correlation function of figure S8a.
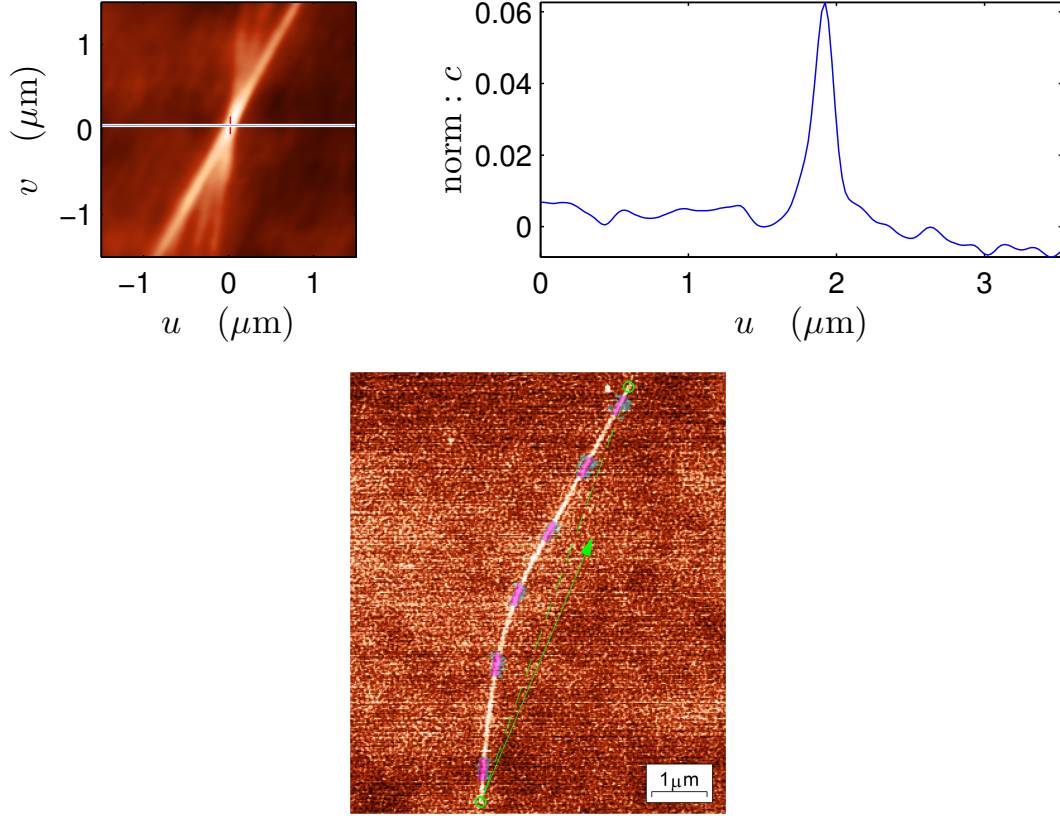

Figure S8: Results from the cross correlation performed in stage 2. (a) The cross-correlation function for $z'_{R2,m}$ in the vicinity of the correlation peak. The location of the peak is shown by the red cross. (b) The value of the cross correlation function along the white line of (a) (c) $z_{R2,m}$ overlaid in purple onto z_{R1}. The green arrow represents a vector whose x and y components equal the correlation error scaled by 0.1μm per 1nm of error. The green dashed line is drawn between the two ends of the nanowire as a guide to the eye.

The effect of tip "convolution"

The finite size of the AFM tip introduces artifacts into topography images. In this section we will consider the impact of so-called tip "convolution" on the detection of features buried beneath spin coated films. If the shape of the AFM tip is known the measured topography may be "deconvolved" to yield the true topography[5] using the approach demonstrated graphically in figure S9a. A copy of the tip's profile (red curve, figure S9a) is placed at each measured position (black solid curve, figure S9a). For each x position the lowest point on each of these tip profiles is then taken as the actual sample topography (black dashed line, figure S9a). As shown in figure S9b the finite size of the tip results in a measured topography which exaggerates the width of the feature. Figure S9c shows how this error increases with falling feature width. It is also apparent that once the feature width exceeds the tip radius by an order of magnitude the tip convolution effect may be safely neglected.
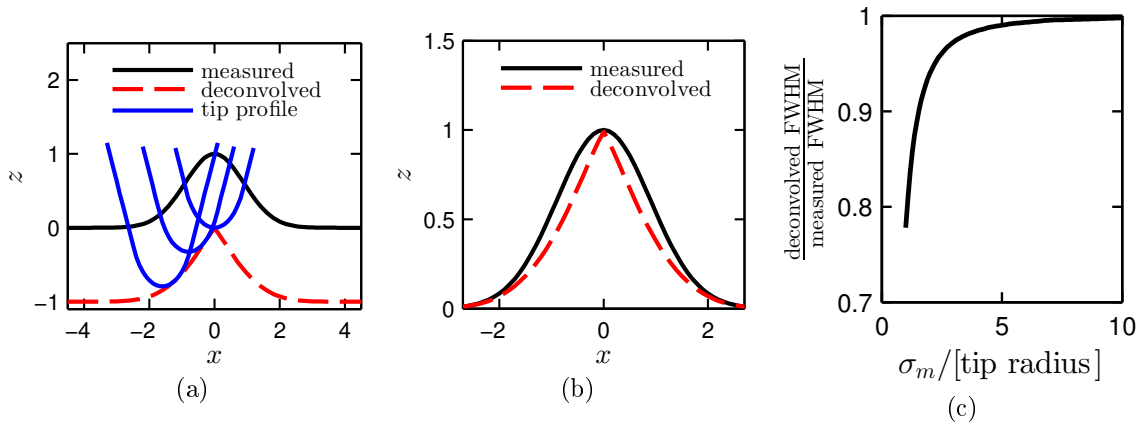

Figure S9: Deconvolution of AFM cross-sections assuming a tip with a 30° cone angle and a spherical end of radius R = 1. The measured cross section was taken to be the Gaussian function, $z = \exp(-x^2/(2\sigma_m^2))$. (a) Graphical demonstration of the deconvolution process whereby a copy of the tip is placed at each position in the measured cross-section (black solid curve). For clarity only three tip positions are shown here (red curves). The deconvolved profile (black dashed line) is then obtained by taking the lowest point from this set of curves. (b) Comparision between the measured and deconvolved cross-sections for $\sigma_m = 0.9$. (c) The dependence on σ_m of the full-width at half maximum (FWHM) of the deconvolved profiles.

Figure S10a shows an SEM micrograph of one of the homemade tSPL tips used in this work. These probes have a typical radius of 5nm and cone angles of roughly 30°. The result

of deconvolving the cross-section of figure 4d with this tip profile is shown in figure S10b. The measured and deconvolved profiles are virtually identical. This is consistent with figure S9c. Figure S10c shows a simulation of the measured topography for the nanowire of figure 4 prior to the spin coating. The two curves in figure S10c are significantly different with errors arising both from the finite slope of the tip and the finite radius. From figures S10b and S10c it can be seen that the planarising effect of spin coating on surface topography reduces the effect of tip convolution.

Indeed for the resist systems we have looked at the characteristic flow length scale σ exceeded the tip radius by more than an order of magnitude. As such the effect of tip convolution can be anticipated to be negligible when measuring the topography of such films. Finally it is worth noting that the tip convolution effect does not itself lead to errors in detecting the position of buried feature. Probe assymetry is required for the introduction of an offset into the measured position of the surface feature. However, in the case where the tip convolution effect is negligible the effect of probe assymetry is likewise negligible.
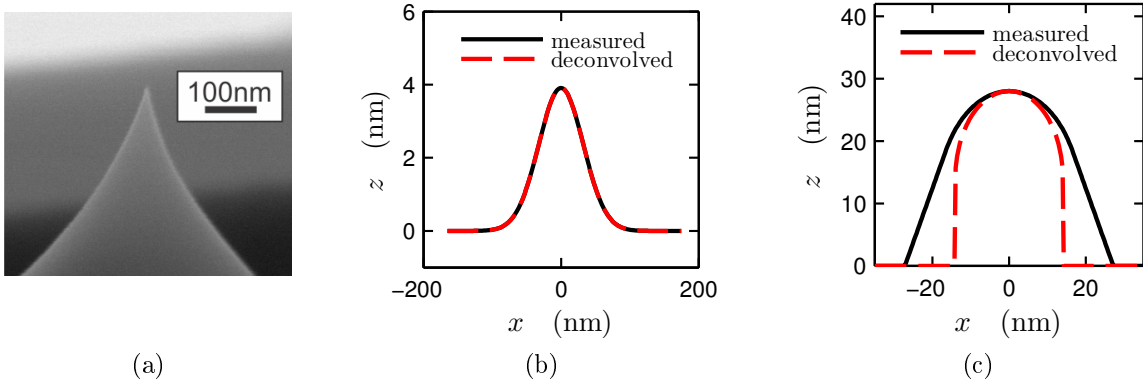

(a) (b) (c)

Figure S10: Deconvolution of the topography over the buried silicon nanowire. (a) SEM micrograph showing the tip of a homemade tSPL cantilever. (b) The result (red dashed line) of deconvolving the fit to the measured AFM cross-section (black line) of figure 4d assuming a tip radius of 5nm. (c) Simulation of the measured and deconvolved topography for the 28nm diameter nanowire.

References

1. Wolf, H.; Rawlings, C.; Mensch, P.; Hedrick, J. L.; Coady, D. J.; Duerig, U.; Knoll, A. Sub 20 nm Silicon Patterning and Metal Lift-Off Using Thermal Scanning Probe Lithography. *J. Vac. Sci. Technol., B* **2015**, *33*, 02B102.

2. Cheong, L. L.; Paul, P.; Holzner, F.; Despont, M.; Coady, D. J.; Hedrick, J. L.; Allen, R.; Knoll, A. W.; Duerig, U. Thermal Probe Maskless Lithography for 27.5 nm Half-Pitch Si Technology. *Nano Lett.* **2013**, *13*, 4485–4491.

3. Rawlings, C.; Duerig, U.; Hedrick, J.; Coady, D.; Knoll, A. Nanometer Accurate Markerless Pattern Overlay Using Thermal Scanning Probe Lithography. *IEEE Trans. Nanotechnol.* **2014**, *13*, 1204–1212.

4. Guizar-Sicairos, M.; Thurman, S. T.; Fienup, J. R. Efficient Subpixel Image Registration Algorithms. *Opt. Lett.* **2008**, *33*, 156–158.

5. Markiewicz, P.; Goh, M. C. Atomic Force Microscopy Probe Tip Visualization and Improvement of Images Using A Simple Deconvolution Procedure. *Langmuir* **1994**, *10*, 5–7.